Invited Paper

Integrated ray tracing simulation of annual variation of spectral bio-signatures from cloud free 3D optical Earth model

Dongok Ryu[*a,b], Sug-Whan Kim[a,b], Dae Wook Kim[c], Jae-Min Lee[d], Hanshin Lee[e] ,Won Hyun Park[c], Sehyun Seong[a,b], Sun-Jeong Ham[d]

[a]Space Optics Laboratory, Yonsei University / Korea, Republic of;

[b]Institute of Space Science and Technology, Yonsei University / Korea, Republic of;

[c]College of Optical Sciences, University of Arizona / United States of America;

[d]'Atmospheric, Oceanic and Planetary Physics' and 'Astrophysics', University of Oxford / United Kingdom;

[e]McDonald Observatory, University of Texas at Austin / United States of America;

ABSTRACT

Understanding the Earth spectral bio-signatures provides an important reference datum for accurate de-convolution of collapsed spectral signals from potential earth-like planets of other star systems. This study presents a new ray tracing computation method including an improved 3D optical earth model constructed with the coastal line and vegetation distribution data from the Global Ecological Zone (GEZ) map. Using non-Lambertian bidirectional scattering distribution function (BSDF) models, the input earth surface model is characterized with three different scattering properties and their annual variations depending on monthly changes in vegetation distribution, sea ice coverage and illumination angle. The input atmosphere model consists of one layer with Rayleigh scattering model from the sea level to 100 km in altitude and its radiative transfer characteristics is computed for four seasons using the SMART codes. The ocean scattering model is a combination of sun-glint scattering and Lambertian scattering models. The land surface scattering is defined with the semi empirical parametric kernel method used for MODIS and POLDER missions. These three component models were integrated into the final Earth model that was then incorporated into the in-house built integrated ray tracing (IRT) model capable of computing both spectral imaging and radiative transfer performance of a hypothetical space instrument as it observes the Earth from its designated orbit. The IRT model simulation inputs include variation in earth orientation, illuminated phases, and seasonal sea ice and vegetation distribution. The trial simulation runs result in the annual variations in phase dependent disk averaged spectra (DAS) and its associated bio-signatures such as NDVI. The full computational details are presented together with the resulting annual variation in DAS and its associated bio-signatures.

Keywords: Disk Averaged Spectrum(Spectra), Full 3D Earth Model, Extra-solar Planet, Terrestrial Planet Finding, Integrated Ray Tracing, Spectral Bio-signature of the Earth, Earth Observing Simulation, Astrobiology

1. INTRODUCTION

Studying spectral bio-signatures from potential earth-like planets in other star systems has attracted great attention from the astrobiology community recently. One of the technical challenges facing the researchers in this field would be accurate de-convolution of measured spectrum collapsed (spatially and temporally) into a single detector pixel of the instruments even for TPF and Darwin missions. Therefore, understanding the Earth disk averaged spectral signatures, as the unique life bearing planet we know as of today, offers an important reference datum for accurate spectral de-convolution.

There have been two approaches to the study of disk averaged spectrum (DAS) of the Earth. First, as for the simulation studies, Ford et al.[1](2001) simulated the diurnal variation of earth light curve by Monte Carlo integrations. The work was followed by Tinetti et al.[2,3](2006a, 2006b)'s computation of synthetic DAS, using Spectral Mapping Atmospheric Radiative Transfer (SMART) model. The DAS was computed for variation of cloud coverage, illumination phase and geometric configurations. Their simulated spectrum averaged over the daily time scale with various cloud coverage

* antinneo@gmail.com; phone 82-2-2123-4247; cell phone 82-10-9096-2010; fax 82-2-392-7680

Instruments, Methods, and Missions for Astrobiology XIII, edited by Richard B. Hoover, Gilbert V. Levin, Alexei Yu. Rozanov, Paul C. W. Davies, Proc. of SPIE Vol. 7819, 78190E

· doi: 10.1117/12.860706

showed well known 'red-edge' signals indicative of surface vegetation from the Earth. In the meantime, Fujii et al.[4](2010) constructed simulated light curves of the Earth model while considering ocean scattering, parameterized land bidirectional reflectance distribution function(BRDF), and cloud-free atmosphere with Rayleigh scattering characteristics. The second approach is spectral measurements. Examples may include, but not limited to, measured spectrum of the earthshine and moon light by Woolf et al.[5](2002). The resulting observation data show clear Rayleigh scattering effects of atmosphere and the 'red-edge' signals for vegetation surface, while atmospheric aerosol and ocean scattering effects were less visible. Furthering this line of study, Montañés-Rodríguez et al.[6](2006) observed earthshine spectra and determined a correlation between the 'red-edge' signal variation and changes in cloud-free vegetation area.

In our earlier work, Ryu et. al.[7,8](2009a, 2009b) introduced a new DAS computation method with a 3D optical Earth model, contributing to technology evolution along the first approach. The core computation is Integrated Ray Tracing (IRT) capable of simultaneous computation of both imaging and radiometric transfer using Monte-Carlo ray tracing. Whilst the earlier model used Lambertian surface (land and ocean) scattering, the work showed computational validity that the IRT model resulted in comparable Earth DAS with other studies for seasonal changes, daily rotation and orbital orientations. Evolving further from the earlier works, this study is aimed at seasonal variations in phase dependent DAS and its vegetation signatures. Especially the computation technique uses, for the first time, the integration of semi-empirical and non-isotropic (i.e. non Lambertian) scattering models for the Earth elements such as atmosphere, land and ocean. This paper describes the concept of the improved IRT computation in Section 2. This is followed by construction of the improved 3D earth mode with non-Lambertian scattering models in Section 3. Section 4 shows the model performances in imaging and radiative transfer computation. The trial simulation runs for DAS and associated bio-signatures are reported in Section 5, before their implications summarized in Section 6.

2. METHODOLOGY – INTEGRATED RAY TRACING MODEL

2.1 Concept of Integrated Ray Tracing computation

The initial version of Integrated Ray Tracing (IRT) model was originally developed as an end-to-end performance simulation tool for satellite instruments.[9] The current model incorporates improvements in the Earth components (listed in Table 1) including non-Lambertian scattering surfaces. In the model, the three elements (i.e. source, target and instrument) are integrated into single Monte-Carlo ray tracing computation flow as listed in Table 2 and shown in Figure 1. The IRT computation flow starts from the sequence 1 and progresses in step by step manner to the sequence 7 in Table 2.

Table 1. Summary of IRT Model Elements

Model	Sun Model	Earth System Model			Instrument Model
Sub-Model		**Atmosphere**	**Land**	**Ocean**	
Radius	695500 km	6499.000 km	6400.767 km	6400.000 km	29 mm
Primary Position	(0,0,1.496E8) km	(0,0,0) km	(0,0,0) km	(0,0,0) km	(0,0,1.5E6) km
Movement	Distance Variation 4 Seasons	Spherical Rotation	Spherical Rotation	Spherical Rotation	Rotation around Earth
Surface Shape	Hemisphere	Spherical Surface with Latitudinal Distribution	Spherical Surface with Bounded Coastline and Vegetation	Sphere Sea Ice Cap	Cassegrain Telescope with Catadioptric system
Surface Optical Characteristic	Lambertian Scattering	Atmospheric Transmittance + Rayleigh Scattering	Non-Lambertian Scattering with Directional Parameter (K_{n_λ})	Lambertian Scattering + Sun-glint Scattering	Reflectance + Transmittance
Surface Composition	1 Layer	18 Latitudinal Layers	6 kinds of Surfaces	1 Layer	Mirrors and Lenses
Surface Variation	None	5 Reference Atmospheric Conditions with 4 Seasons + Continental/Desert/Maritime Aerosols	Seasonal Spectral Directional Parameter from POLDER3/PARASOL Observations	Sea Ice Area Variation (Monthly)	None

Initially, 40,000 light rays are created inside the Sun from using Geymard[10](2004)'s spectral solar constant(W/m^2/nm) (trace sequence 1). They then encounter with the Sun surface, where each ray is scattered into 4 child rays through Lambertian scattering surface (i.e. trace sequence 2). Among those scattered rays, the 120,000 rays emitted within the solid angle defining the Earth sphere are traced. The rays arriving at the Earth experience reflection, transmission and scattering as they pass through atmospheric layer (i.e. trace sequence 3 and 4) twice (i.e. inward and outgoing) and are bounced from the land and ocean surfaces (i.e. trace sequence 5). The rays scattered and emitted out from the top of the atmosphere are traced into the instrument aperture, where they are to pass through the instrument optical train before arriving at the detector plane (i.e. trace sequence 6 and 7). These trace sequences are illustrated in Figure 1.

Table 2. Integrated ray tracing computation flow

	Ray Emitting	**Sun Scattering**	**Atmosphere Transmission**	**Atmosphere Scatter**	**Land / Ocean Surface Scatter**	**Scattering Rays in Aperture**	**Image Plane**
Computation Sequence	1	2	3	4	5	6	7
Object	Inside of Sun	Sun Surface	Atmosphere	Atmosphere	Lands	Aperture	Detector
Rays(n)	40,000	40,000	120,000	40,000	120,000	~160,000	~160,000
Position $P(x,y,z)$	$\|x\| < 695500$km $\|y\| < 695500$km $\|z\| = 1.50$E8km	$\|x\| = 695500$km $\|y\| = 695500$km 1.5E8-6.9E5 < $\|z\| < 1.50$E8km	$\|x\| < 6499$km $\|y\| < 6499$km $0 < \|z\| < 6499$	$\|x\| < 6499$km $\|y\| < 6499$km $0 < \|z\| < 6499$	$\|x\| < 6499$km $\|y\| < 6499$km $0 < \|z\| < 6499$	$\|x\| < 29$mm $\|y\| < 29$mm $z = 1.5$E6 km	Focus $z = 1.5$E6 km
Direction $D(a,b,c)$	Random	Toward Atmosphere	Toward Land and Ocean	Toward TOA or Instrument	Toward TOA or Instrument	Toward Primary Mirror	Focus
Radiant Power (f)	Spectral Radiant Power (W) / n	Lambertian BRDF	Atmospheric Transmittance	Rayleigh BSDF	Non-lambertian BRDF	Sum of scattering	Radiant Power on detector
Status(ε)	Emitting	Scattering	Transmission	Scattering	Scattering	Stored	End Trace

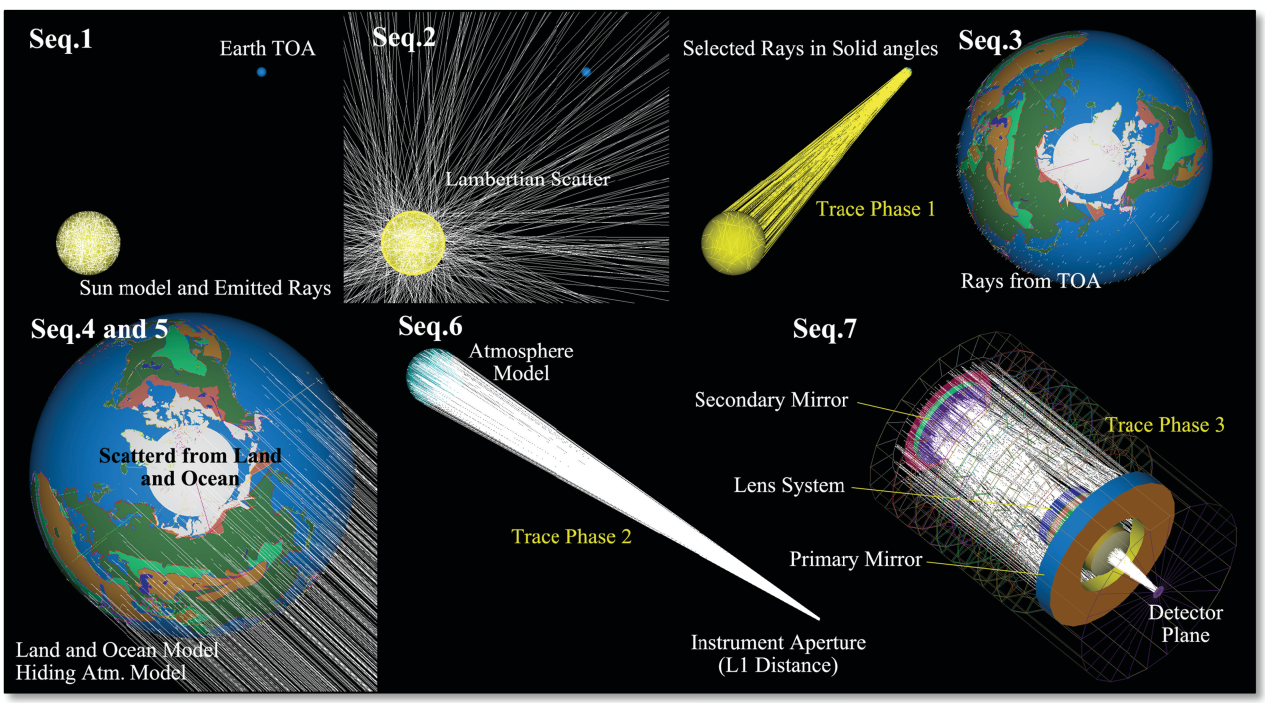

Figure 1. Elements and trace phase in IRT model (Sun/Earth/AmonRa instrument: Ray tracing sequence 1-7)

In the ray tracing computation, a set of ray is defined as in Equation 2.1.[11]

$$\sum_{i=1}^{n} \overrightarrow{\Re_\iota}(\lambda, x, y, z, a, b, c, f, \varepsilon) \tag{2.1}$$

where i is the i^{th} ray, λ wavelength, (x, y, z) global coordinate position, (a, b, c) direction cosine, f radiant power of a ray and ε is ray status (i.e. current object surface, history of object, ray condition – parent, scatter, split ray). In this ray expression, the ray before it encounters an object has subscript "s" and the ray after it experiences with an object has the subscript "v". Following this convention, a set of ray passing an object can be defined as in Equation 2.2 below.

$$\overrightarrow{\Re_v} = \sum_{i=1}^{n} T(\overrightarrow{\Re_{s\_\iota}}) + \sum_{i=1}^{n} R(\overrightarrow{\Re_{s\_\iota}}) + \sum_{i=1}^{n} \Pi(\overrightarrow{\Re_{s\_\iota}}) \tag{2.2}$$

$$\sum_{i=1}^{n} T(\overrightarrow{\Re_{s\_\iota}}) = \sum_{i=1}^{n\times n'} \overrightarrow{\Re_{v\_\iota}}(\lambda, P_T(x, y, z), D_T(a, b, c), f_s T, \varepsilon_T) \tag{2.3}$$

$$\sum_{i=1}^{n} R(\overrightarrow{\Re_{s\_\iota}}) = \sum_{i=1}^{n\times n'} \overrightarrow{\Re_{v\_\iota}}(\lambda, P_R(x, y, z), D_R(a, b, c), f_s R, \varepsilon_R) \tag{2.4}$$

$$\sum_{i=1}^{n} \Pi(\overrightarrow{\Re_{s\_\iota}}) = \sum_{i=1}^{n\times n''} \overrightarrow{\Re_{v\_\iota}}(\lambda, P_\Pi(x, y, z), D_\Pi(a, b, c), F_v, \varepsilon_\Pi) \tag{2.5}$$

where n' is the number of split rays (for Equation 2.3 and 2.4) per each parent ray and n'' is the number of scattered rays (for Equation 2.5) per each parent ray. The object surface has reflectance (Equation 2.3), transmittance (Equation 2.4) and bidirectional scattering distribution function (BSDF in Equation 2.5). For each and every ray encounter with an object, the total energy conservation is applied as expressed in Equation 2.6,

$$A = 1 - [R + T + TIS] \tag{2.6}$$

where A is absorption and TIS means total integrated scatter (TIS) defined as in Equation 2.7.[12]

$$\mathrm{TIS}(\theta_s, \theta_s) = \int_0^{2\pi} \int_0^{\pi/2} BSDF(\theta_s, \theta_v, \phi_s, \phi_v) \cos\theta_v \sin\theta_v \, d\theta_v d\phi_v \tag{2.7}$$

In the meantime, radiant power f_v when experiencing scattering can be defined as in Equation 2.8.[12]

$$f_v = f_s BSDF(\theta_s, \theta_v, \phi_s, \phi_v) \frac{A \cos\theta_e \cos\theta_v}{n'' R^2} \tag{2.8}$$

where θ_s is incident zenith angle, θ_v scattering zenith angle, ϕ_s incident azimuth angle and ϕ_v scattering azimuth angle.

3. EARTH MODEL CONSTRUCTION

3.1 Atmospheric Sub-Model and Seasonal Variation

The Earth atmosphere is defined with 18 sub components as drawn in Figure 2 and each component is defined with Spectral Mapping Atmospheric Radiative Transfer (SMART) model[13,14] and with continental, maritime[15] and desert[16] aerosol models. In addition, NASA Earth Observation (NEO) database[17] was used to obtain disk averaged CO_2 concentration and aerosol optical depth at 550nm for the period of Nov. 2005 – Oct 2006. For characterizing the atmospheric transmittance, spectral atmospheric transmittance (except for Rayleigh transmittance) was used. For reflectance, Rayleigh scattering was considered as its BSDF is expressed in Equation 3.1 from Fujii et al.[4](2010).

$$BSDF_{rayleigh}(\theta_s, \theta_v, \phi, \lambda) = \frac{\pi\omega\Psi(\xi)}{\cos\theta_s + \cos\theta_v}\left[1 - exp\left\{\tau_R(\lambda)\left(\frac{1}{\cos\theta_s} + \frac{1}{\cos\theta_v}\right)\right\}\right] \tag{3.1}$$

where $\Psi(\xi)$ is Rayleigh scattering phase function, ξ phase angle (angle between the incident and scattered direction) and $\tau_R(\lambda)$ optical depth for Rayleigh scattering defined as in Equation 3.2[4]

$$\tau_R(\lambda) = 0.00864\left(\frac{P}{1013.25mbar}\right)\lambda^{-\left(3.16+0.074\lambda+\frac{0.05}{\lambda}\right)} \tag{3.2}$$

In here, ω is spectral atmospheric transmittance (except for Rayleigh scattering) accounting for ozone (T_{o_λ}), nitrogen (T_{n_λ}), other mixed gas (T_{g_λ}), water vapor (T_{w_λ}) and aerosols (T_{a_λ}) and it can be expressed as in Equation 3.3.[14]

$$\omega = T_{o\_\lambda}T_{n\_\lambda}T_{g\_\lambda}T_{w\_\lambda}T_{a\_\lambda} \tag{3.3}$$

Using Equation 3.1, atmospheric BSDF was computed and an example of the resulting BSDF data is presented in Figure 3.

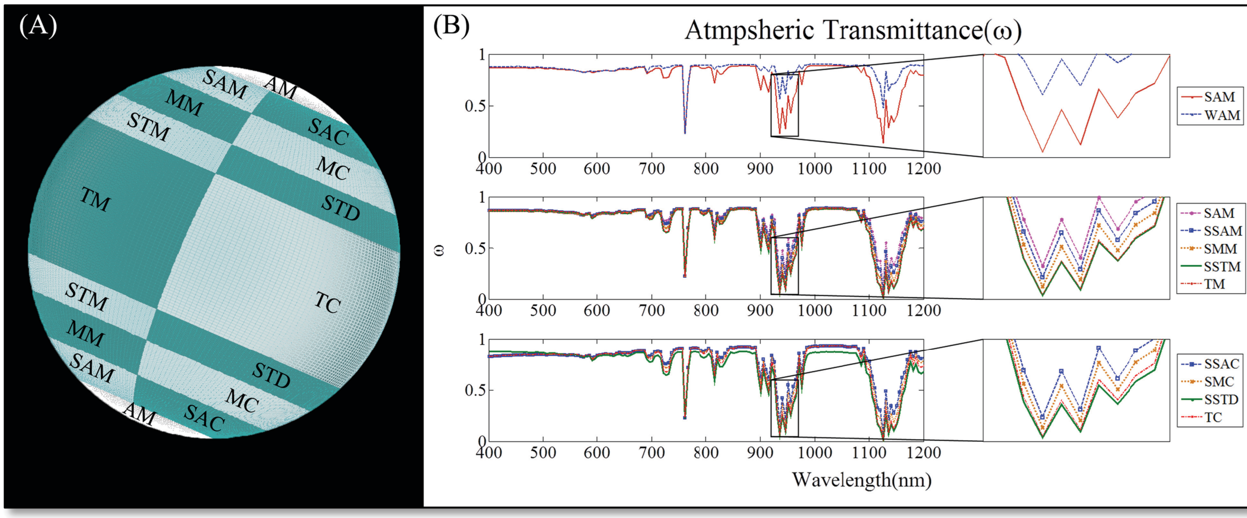

Figure 2. **(A)**: Longitudinal atmospheric structure (A: arctic, SA: sub-arctic, M: mid-latitude, ST: sub-tropic, T: tropical/ last letter: maritime(M), continental(C), desert(D) aerosol model) **(B)**: Atmospheric transmittance (first letter: Winter(W)/summer(S)) and zoom in H_2O absorption line from 920nm to 970nm

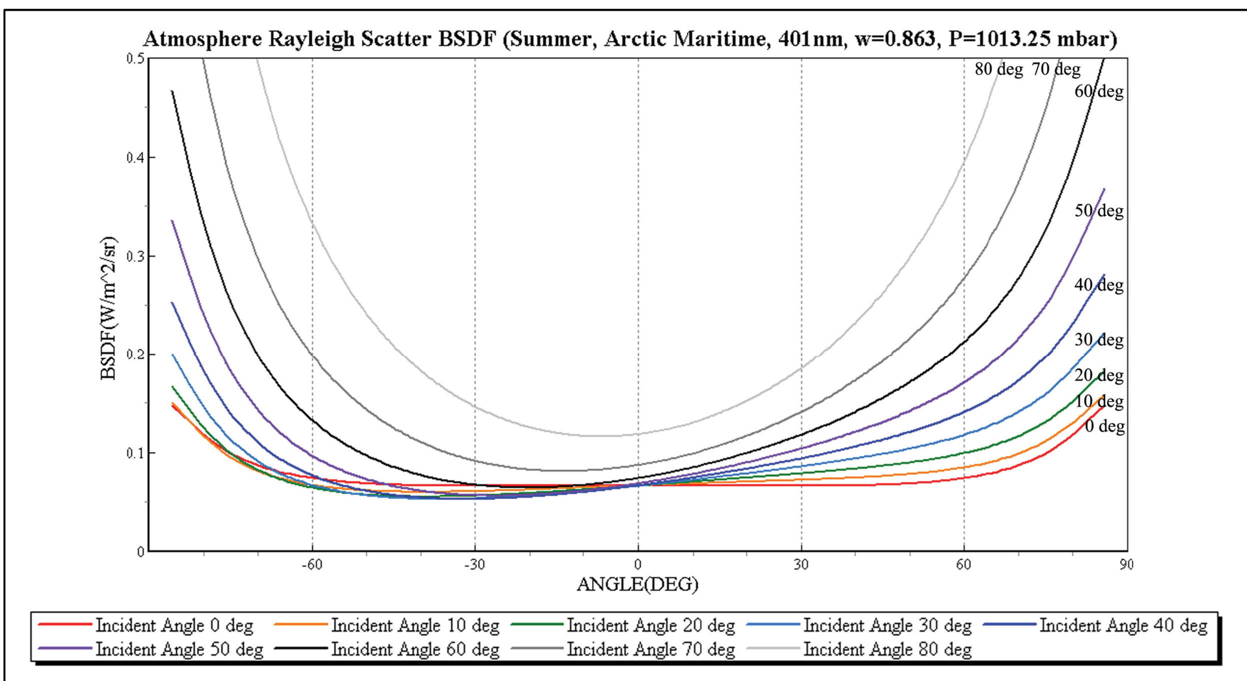

Figure 3. Atmospheric Rayleigh scatter BSDF (example case; summer, arctic maritime, 401nm, w=0.863, P=1013.25mBarr)

3.2 Land Sub-Model and Seasonal Variations

The land sub-component consists of 3D polygon surfaces with spherical curvature and it is divided into 5 different types (including ice, tundra, forest, grass, and ground) of vegetation and non-vegetation surfaces using Global Ecological Zone (GEZ) map[18]. For each surface type, a non-Lambertian spectral BRDF is defined using a semi empirical parametric kernel model used for MODIS and POLDER missions as expressed in Equation 3.4.[19,20]

$$BRDF(\theta_s, \theta_v, \phi, k_{i\_\lambda})\pi = K_{0\_\lambda} + K_{1\_\lambda}F_1(\theta_s, \theta_v, \phi) + K_{2\_\lambda}F_2(\theta_s, \theta_v, \phi) \tag{3.4}$$

where K_{0_λ} is isotropic (Lambertian) scattering, K_{1_λ} geometrical roughness indicator (shadow effect) and K_{2_λ} volume scattering indicator. $F_1(\theta_s, \theta_v, \phi)$ is reciprocal geometric kernel of "Li_sparse" defined by Lucht et al.[21](2000) and $F_2(\theta_s, \theta_v, \phi)$ is volumetric kernel of "Ross_thick" defined by Roujean et al.[22](1992) merged with a hotspot module suggested by Breon et al.[23](2002). Using the level 3 data set of the POLDER-3/PARASOL instrument, we obtained K_{0_λ}, K_{1_λ} and K_{2_λ} for the period of Nov. 2005 – Oct 2006, and examples of computed K_{0_λ} are illustrated in Figure 4. Employing Equation 3.4, K_{0_λ} value of each land surface BRDF was obtained and is illustrated in Figure 5 and they were then imported into the IRT computation.

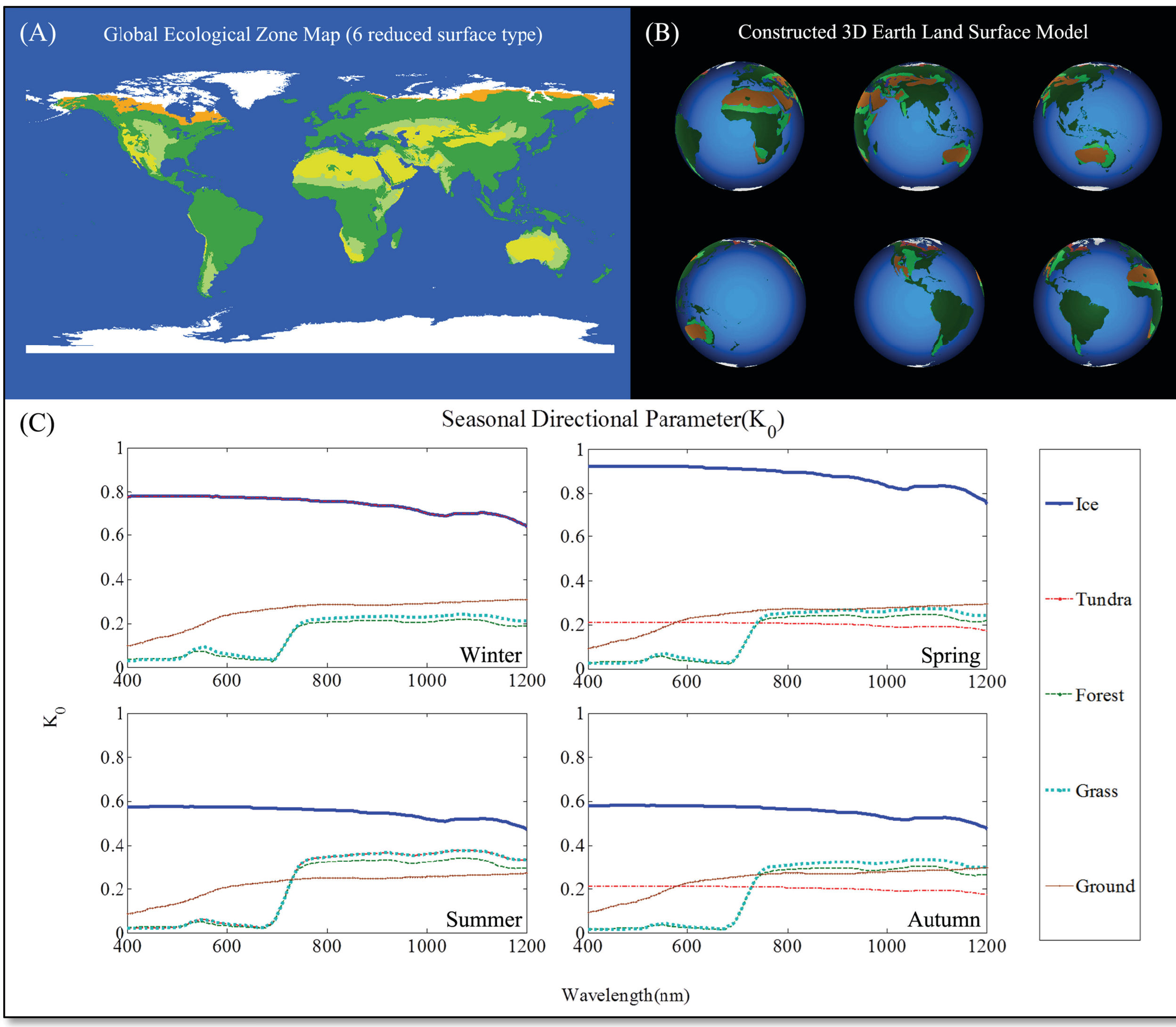

Figure 4. (A): Global ecological zone map (B): Constructed 3D land surface model (C): Example of seasonal directional parameter K_0

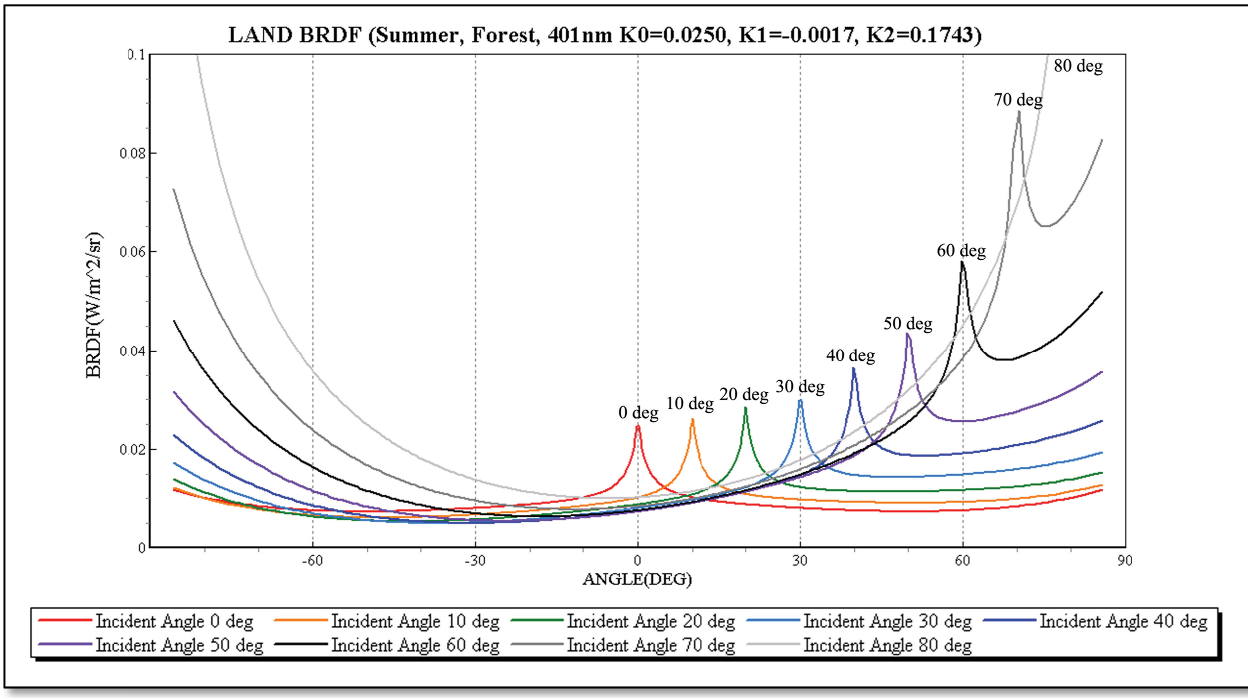

Figure 5. Land BRDF model (example case; summer, forest, 401nm, K_0=0.0250, K_1=-0.0017, K_2=0.1743)

3.3 Ocean Sub-Model and Seasonal Variations

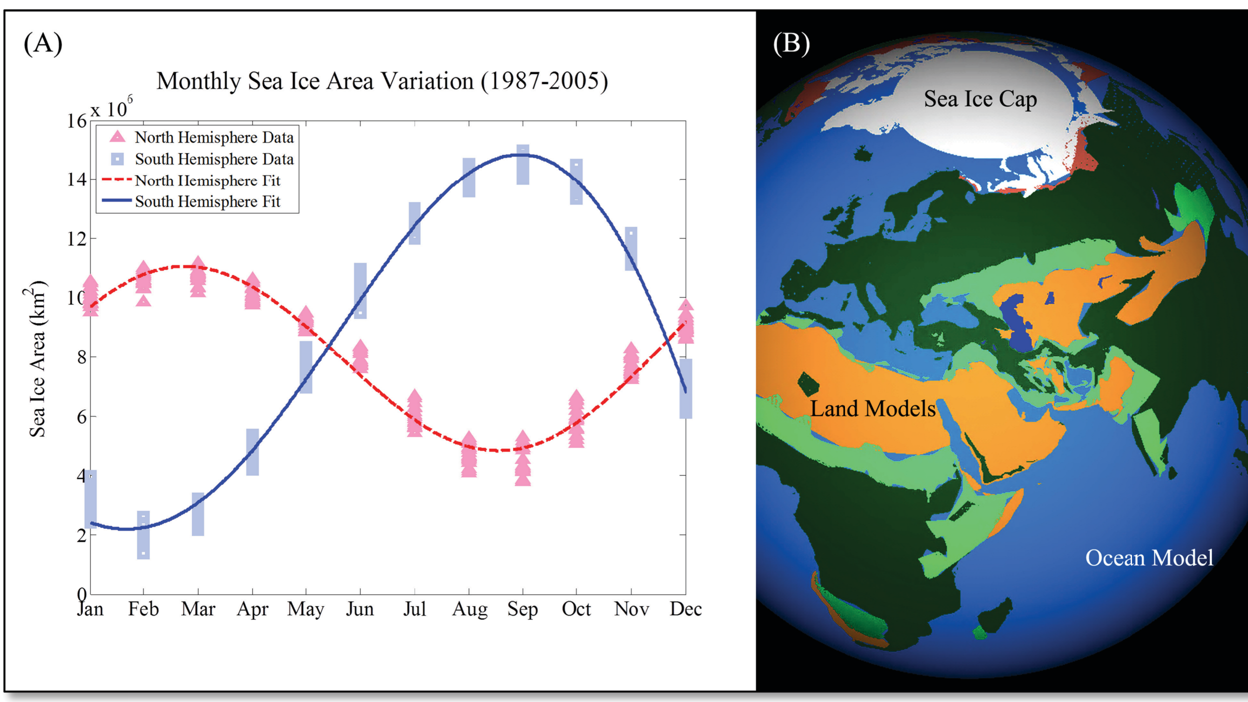

Figure 6. (A): Sea ice area variations (B): Sea ice cap with land and ocean model

The ocean sub component model consists of two parts. They are a spherical surface layer covering the earth globe and the sea ice caps around the north and south poles. Using the annual average data over the period of 1987-2005 from Snow and Ice Data Center (NOAA)[24], the monthly variation of sea ice area is modeled as illustrated in Figure 6. The scattering characteristics of sea ice caps is the same BRDF model as the land ice and described in Equation 3.4 in Section 3.2 whereas the ocean surface BRDF model is defined as in Equation 3.5.

$$BRDF_{Ocean}(\theta_s, \theta_v, \phi, \lambda) = BRDF_{Lambertian\_\lambda} + BRDF_{sun-glint}(\theta_s, \theta_v, \phi, \lambda) \quad (3.5)$$

The $BRDF_{Lambertian\_\lambda}$ term is defined with the ocean spectral albedo (i.e. TIS of $BRDF_{Ocean}(\theta_s, \theta_v, \phi, \lambda)$) from Tinetti et al.[2](2006a) subtracted by the computed TIS of the Sun-glint scatter model expressed in Equation 3.6. For $BRDF_{sun-glint}(\theta_s, \theta_v, \phi, \lambda)$, the ocean scatter model from Fujii et al.[4](2010) and Nakajima et al.[25](1983) expressed in Equation 3.6 was used to approximate the global ocean scattering by accumulating scattering contributions from small wave facets.[4]

$$BRDF_{sun-glint}(\theta_s, \theta_v, \phi, \lambda) = \frac{1}{4\cos\theta_s \cos\theta_v \cos\theta_n{}^*} p(\theta_n{}^*, u_{10}) G(\theta_s, \theta_v, \phi, u_{10}) r(n, \theta_s, \theta_v, \phi) \quad (3.6)$$

where θ_n and ϕ_n are normal direction to the ocean wave facet created by wind, $p(\theta_n{}^*, u_{10})$ empirical density distribution function of wave slope, $G(\theta_s, \theta_v, \phi, u_{10})$ bidirectional shadowing effect, u_{10} wind speed at 10 m above the ocean, $r(n, \theta_s, \theta_v, \phi)$ Fresnel's scattering coefficient and n refractive index of water. The realistic ocean scatter data were computed from using Equation 3.5 and an example is shown in Figure 7 where the Lambertian scatter term computed from 0.0598 (i.e. TIS = 19%) for 401 nm in wavelength was added by the Sun glint scattering obtained from u_{10}=4m/s in monthly averaged wind speed at 10m in altitude.[4]

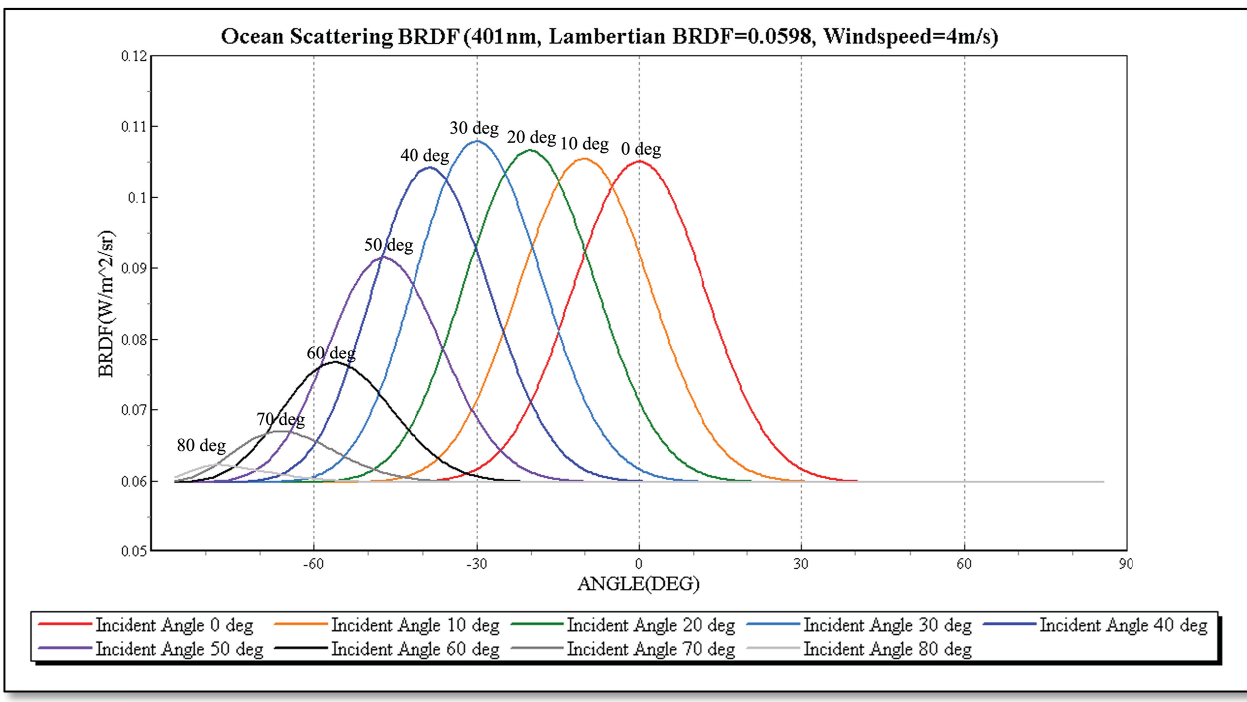

Figure 7. Ocean BRDF model (example case; 401nm, Lambertian BRDF=0.0598, monthly averaged wind speed=4m/s)

4. IRT MODEL VERIFICATION

4.1 Imaging performance verification

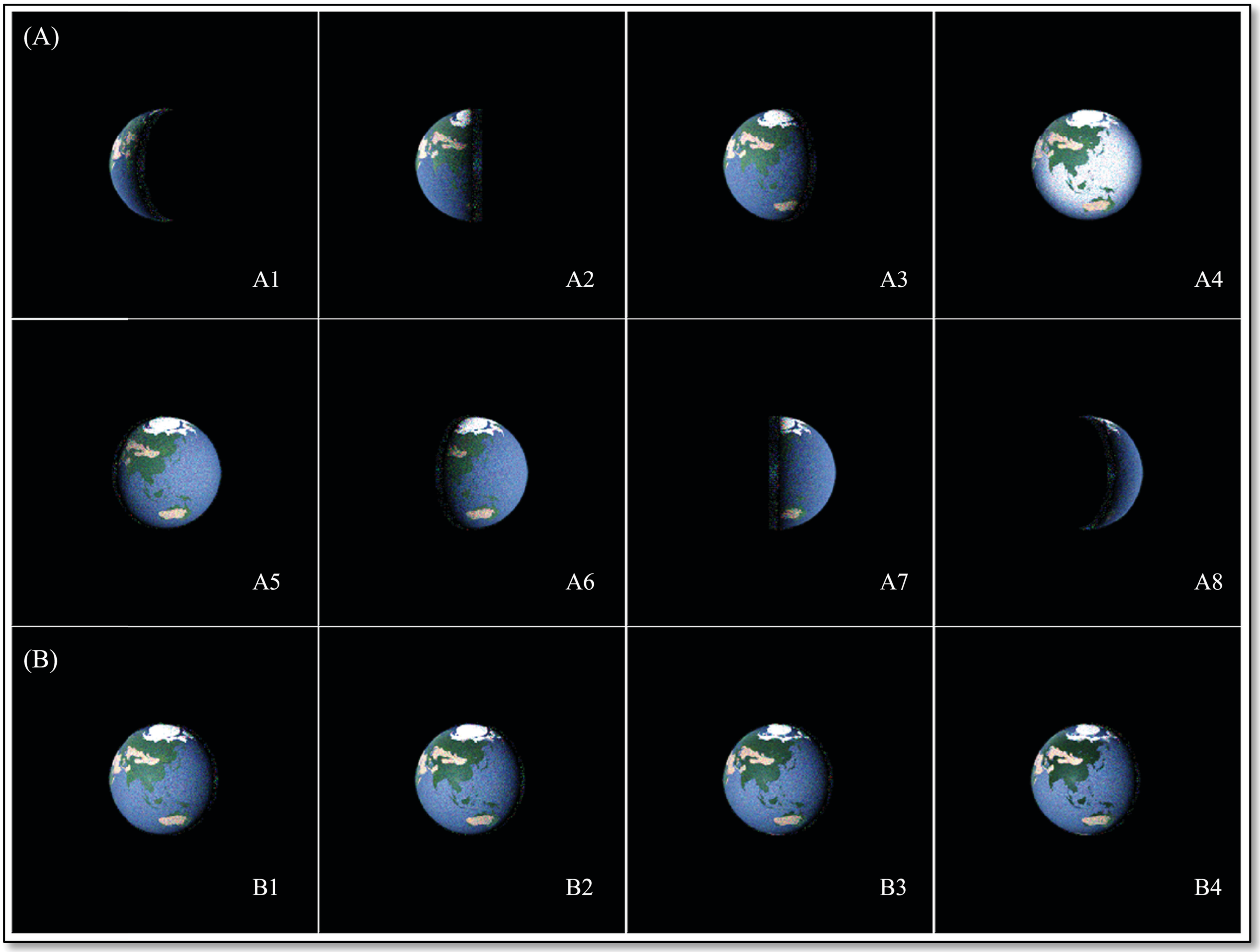

Figure 8. True color images of the Earth model (Center of viewing direction: 120E, 23.5N) at the AmonRa instrument detector plane.

Assuming that the hypothetical AmonRa instrument[7] looks at the Earth from the L1 distance (i.e. 150,000,000 km from the Earth) while maintaining the fixed viewing direction toward (120E, 23.5N) on the Earth surface, the Earth images were computed at 30 degree in illumination phase variation step (i.e. A1 to A8 in Figure 8(A)), each being a RGB composite image obtained from simulation results in 5 wavelength bands (i.e. 451 nm, 491 nm, 521 nm, 566 nm and 651 nm). We note that i) the central part is brighter than the rest of the Earth globe and it is caused by strong sun glint scattered light entering into the instrument aperture, ii) the images show atmospheric scattering features from the shadowy side of the Earth globe, iii) the land surface show uniform scattering while exhibiting weak features of hot spot toward the forward specular direction. Specially, the four images (i.e. B1-B4) in the bottom row represent the Earth globe in seasonal changes from winter to autumn and show the seasonal changes in sea ice cap area around the North Pole and Tundra area as well as its changes in surface color and brightness.

4.2 Radiative transfer performance

For assessing the radiative transfer computation accuracy, the IRT simulation was run for computation of radiant power transfer from the Sun to the Earth (as a Lambertian sphere of 0.3 in uniform albedo) and then from the Earth to the AmonRa instrument aperture. The same computation steps were also performed analytically and the results from both simulation and analytic computation are compared in Figure 9. We note that as long as the number of rays used is greater than 30000, the arriving radiant power difference between the IRT simulation and the analytical computation is kept below ±0.5%. This led to the use of 40000 rays created inside the Sun for the IRT simulation for DAS computation, as mentioned in Section 2.

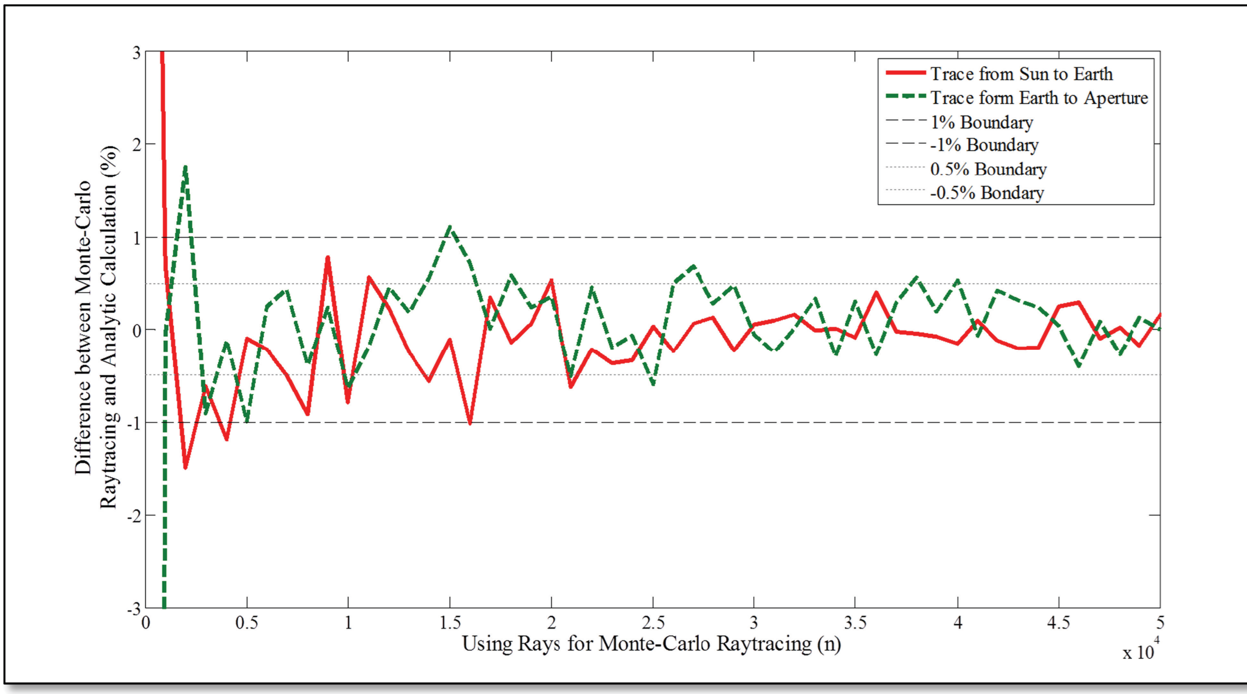

Figure 9. Difference between IRT simulation and analytical computation in arriving radiant power at the AmonRa instrument aperture

5. DISK AVERAGED SPECTRA AND BIO-SIGNATURE DETECTION

5.1 Disk Averaged Spectra

Table.3. IRT simulation cases

Simulation Case	Illuminated Phase	Direction of Earth Viewing Orientation[26]		Seasons	Result Parameter
Case 1	100% Full Illuminated	120E, 23.5N		4	rad/rad$_{top}$ NDVI
Case 2	0% Crescent	120E, 23.5N	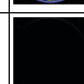	4	rad/rad$_{top}$ NDVI
Case 3	50% Half Illuminated	120E, 23.5N Land Dominance		4	rad/rad$_{top}$ NDVI
Case 4	50% Half Illuminated	120E, 23.5N Ocean Dominance		4	rad/rad$_{top}$ NDVI
Case 5	50% Half Illuminated	30E, 0N Land Dominance		4	rad/rad$_{top}$ NDVI
Case 6	50% Half Illuminated	150W, 0N Ocean Dominance	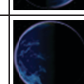	4	rad/rad$_{top}$ NDVI

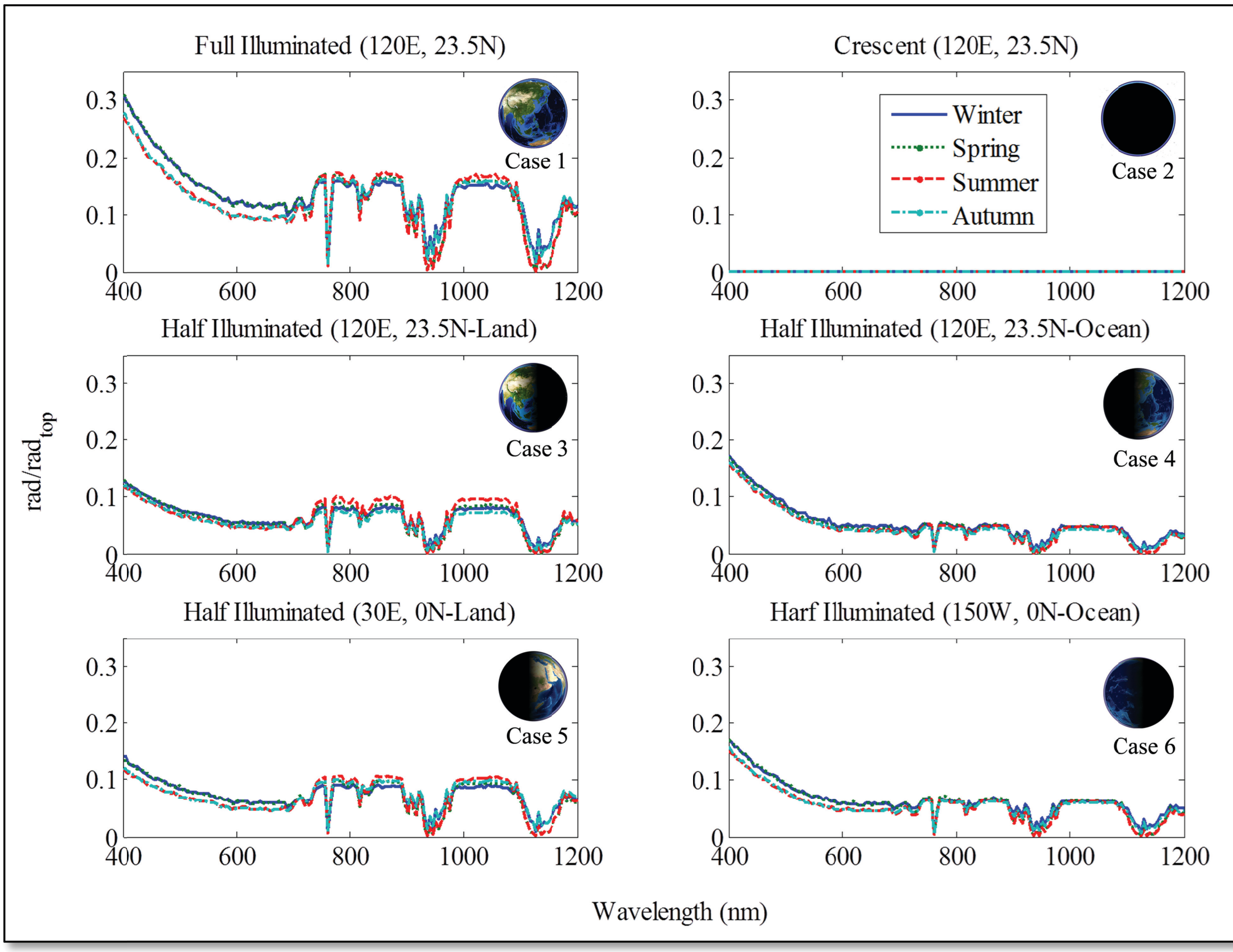

Figure 10. Earth DAS in four seasons and four illumination phases (i.e. full, land dominant half, ocean dominant half and zero)

According to Tinetti et al.[2](2006a), DAS for visible and near infra-red (NIR) can be defined as the ratio of upward radiance(rad) to downward radiance(rad$_{top}$) at the top of the Earth atmosphere and it can be expressed as in Equation 5.1. The equation can then be re-written to more practical form as in Equation 5.2 for IRT simulation based DAS computation. Aided with the aforementioned computational verification, we performed IRT simulation for various cases listed in Table 3 and the resulting DAS are shown in Figure 10.

$$Disk\ Averaged\ Spectra(\theta_s, \theta_v, \phi, \lambda) = \frac{\int_0^{2\pi}\int_0^{\pi/2} L_{TOA\_upward}(\theta_s, \theta_v, \phi_s, \phi_v, \lambda)d\Omega}{L_{TOA\_downward}(\theta_s, \phi_s, \lambda)} \tag{5.1}$$

$$Disk\ Averaged\ Spectra(\lambda) = \frac{\sum_{i=1}^{nn''} \overrightarrow{\Re_{\iota}}_{Earth\ to\ TOA}(\lambda, x_v, y_v, z_v, a_v, b_v, c_v, f_v, \varepsilon_v)}{\sum_{i=1}^{nn''} \overrightarrow{\Re_{\iota}}_{Sun\ to\ TOA}(\lambda, x_s, y_s, z_s, a_s, b_s, c_s, f_s, \varepsilon_S)} = \frac{\sum_{i=1}^{nn''} f_{v\_\lambda}(i)}{\sum_{i=1}^{nn''} f_{s\_\lambda}(i)} \tag{5.2}$$

where Ω is solid angle and $\sum_{i=1}^{nn''} f_{v\_\lambda}(i)$ extracted value of radiant power (W) from set of rays.

From Figure 10, we note that i) absorption lines for Rayleigh scattering, O_2, CO_2 and H_2O are clearly identifiable and ii) the overall magnitude of averaged spectrum is comparable to those of the existing studies[7,8] with the cloud free atmospheric assumption. It is clearly seen that the DAS magnitude decreases from the full illumination to the crescent and this tends to prove the validity of the computational flow. For full illumination case, the well-known 'red-edge' signature is very prominent during the summer as expected from the increased amount of land vegetation. For four half illumination cases, short wavelength (i.e. 400-700 nm) spectral differences are mainly caused by the seasonal variation in the amount of sea ice cap. For the wavelength range over 700 nm, the 'red-edge' feature is sensitive to the seasonal changes in vegetation area and such tendency is very strong for the land dominant case 1, 3 and 5. Looking at the ocean dominant case 4 and 6, DAS tends to increase sharply as the wavelength approaches to 400nm and this corresponds to the ocean albedo increase toward the shorter wavelength. The seasonal difference in 'red-edge' signature becomes almost indistinguishable for the ocean dominant cases. We also note that the water vapor absorption lines for the wavelength range of 900-1000 nm and 1100-1200 nm appear in all illumination cases and they are very prominent during the summer. This is coherent with the seasonal variation of atmospheric transmittance shown in Figure 2. In summary, the resulting DAS from IRT model computation are in good agreement with other studies and with common expectations from seasonal changes in the Earth components including atmospheric transmittance, vegetation and sea ice cap areas.

5.2 Seasonal NDVI and surface type ratio

Normalized Difference Vegetation Index (NDVI) is a vegetation signature and can be expressed as in Equation 5.3

$$NDVI(n) = \frac{Red - NIR(n)}{Red + NIR(n)} \tag{5.3}$$

where Red is spectral magnitude of the wavelength range 651-681 nm (for both $NDVI(1)$ and $NDVI(2)$), $NIR(n)$ 751-801 nm (for $NDVI(1)$) and 856-876 nm (for $NDVI(2)$), following existing studies[3,7,8] The DAS data explained in the previous section was used to derive the NDVI shown in Figure 11, where $NDVI(2)$ is higher than $NDVI(1)$ for all seasons, as $NIR(2)$ spectral magnitude is higher. Specially, both $NDVI(1)$ and $NDVI(2)$ increase by the factor of about two as the season changes from winter to summer. This is a part of general tendency that both $NDVI(1)$ and $NDVI(2)$ are weakest in winter, rises slowly in spring, reaches to the strongest signature in summer before it subsides in autumn. It is also seen that the $NDVI(1)$ and $NDVI(2)$ are weaker in ocean dominant half illumination cases than in land dominant half illumination cases. In general, our study shows that the computed NDVI ranges from -0.152 to 0.136 and the winter NDVIs are somewhat close to -0.05~0.08 for full illumination case and -0.07 ~0.1 for half illumination case reported by Tinetti et.al.[3](2006a). Figure 12 shows surface type ratio versus NDVI for four surface types (i.e. forest, grass, ice and ocean). It is clearly shown that the surface type ratio for vegetation area (i.e. forest and grass) has strong positive correlation with the NDVI, whereas non-vegetation surfaces have somewhat vague (ground) and negative (ocean) correlation with the NDVI.

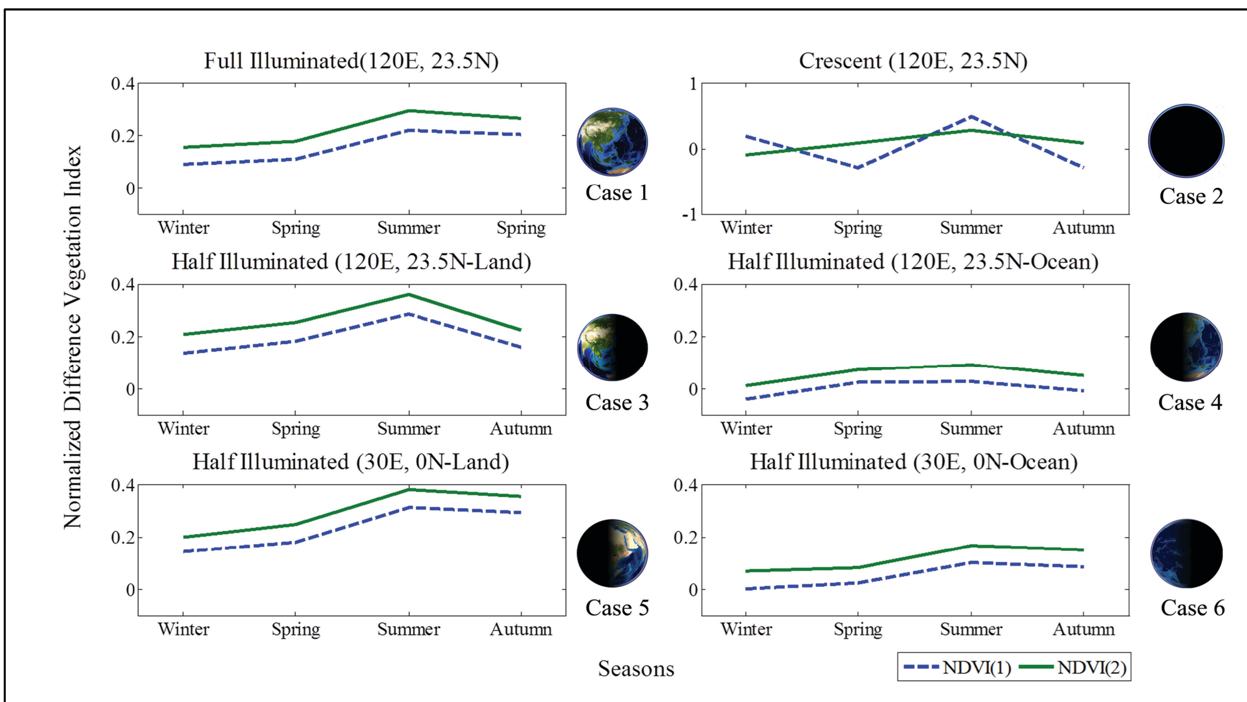

Figure 11. Seasonal NDVI variation and illumination phase

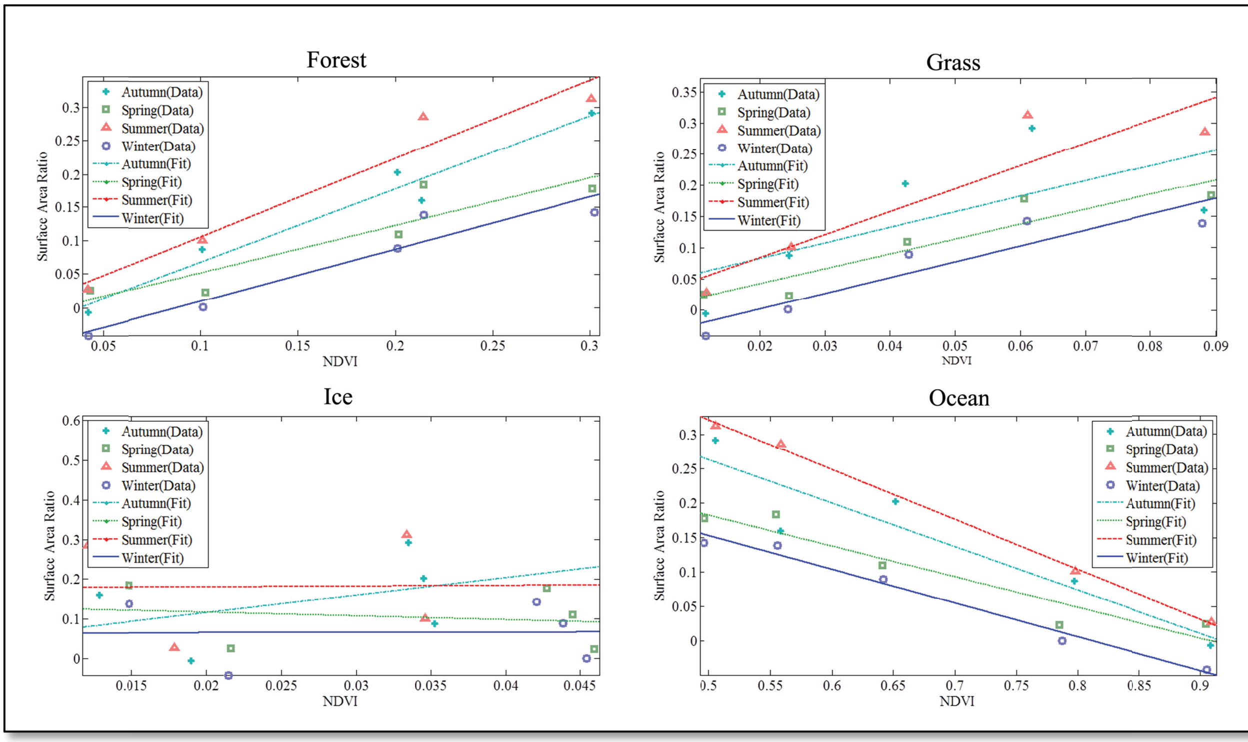

Figure 12. Seasonal NDVI vs. Area ratio of surface types

6. CONCLUDING REMARKS

This study presents a new 3D Earth model equipped with semi-empirical and non-isotropic scattering models for its components (i.e. atmosphere, land and ocean) and the resulting DAS and its associated bio-signatures based on the IRT model computation. In particular, the model computation is benefitted from the use of seasonal changes in scattering characteristics of the Earth components as well as variation in illumination phase. The computed DAS show good agreement with other existing studies and with the common expectations from the seasonal surface changes such as vegetation area and sea ice cap area. From NDVI analysis, our study shows that the increasing vegetation area in summer tends to increase NDVI whereas it decreases during the winter and that there are strong positive correlation between NDVI and surface type ratio at least for the vegetation area (i.e. forest and grass). On the other hand, non-vegetation surfaces have unclear (ground) and negative (ocean) correlation with the NDVI. This proves that the current NDVI definition is reasonable for bio-signature detection from potential extra-terrestrial planets in other star systems.

REFERENCES

[1] E. B. Ford, S. Seager and E. L. Turner, "Characterization of Extrasolar Terrestrial Planets from Diurnal Photometric Variability", Nature 412, 885-887 (2001)

[2] Giovana Tinetti, Victoria S. Meadows, David Crisp, William Fong, Evan Fishbein, Margaret Turnbull, and Jean-Pierre Bibring, "Detectability of Planetary Characteristics in Disk-Averaged Spectra. I: The Earth Model", Astrobiology 6(1), 34-47 (2006)

[3] Giovana Tinetti, Victoria S. Meadows, David Crisp, Nancy Y. Kiang, Brian H. Kahn, Emmaneul Bosc, Evan Fishbein, Thangasamy Velusamy and Margaret Turnbull, "Detectability of Planetary Characteristics in Disk-Averaged Spectra II: Synthetic Spectra and Light-Curves of Earth", Astrobiology 6(6),881-900 (2006)

[4] Yuka Fujii, Hajime Kawahara, Yasushi Suto, Atsushi Tarura, Satoru Fukuda, Teruyuki Nakajima and Edwin L. Turner, "Colors of a Second Earth : Estimation the Fractional Areas of Ocean, Land, and Vegetation of Earth-like Exoplanets", ApJ 715, 866-880 (2010)

[5] N. J. Woolf, P. S Smith, W. A. Traub and K. W. Jucks, “The Spectrum of Earthshine: A Pale Blue Dot Observed from the Ground”, ApJ 574, 430-433 (2002)
[6] Pilar Montañés-Rodríguez, E. Pallé, P. R. Goode and F. J Martín-Torres, “Vegetation Signature in the Observed Globally Integrated Spectrum of Earth Considering Simulatneous Cloud Data : Applications for Extrasolar Planets”, ApJ 651, 544-552 (2006)
[7] Dongok Ryu, Sehyun Seong, Jae-Min Lee, Jinsuk Hong, Soomin Jeong, Yukyeong Jeong and Sug-Whan Kim, “Integrated Ray Tracing Simulation of Spectral Bio-signatures from Full 3-D Earth Model”, Proc. SPIE 7441, 74410A-1-11 (2009)
[8] Dongok Ryu, Sehyun Seong, Jae-Min Lee, Jinsuk Hong, Soomin Jeong, Yukyeong Jeong and Sug-Whan Kim, “Integrated Ray Tracing Simulation of Spectral Bio-signature form Full 3-D Earth with Simple Atmospheric Models and Sea Ice Coverage Variation”, Workshop on Astronomical Instrumentation 3,39-44 (2010)
[9] Sehyun Seong, Jinhee Yu, Dongok Ryu, Jinsuk Hong, Jee-Yeon Yoon, Sug-Whan Kim, Jun-Ho Lee, and Myung-Jin Shin, “Imaging and radiometric performance simulation for a new high-performance dual-band airborne reconnaissance camera”, Proc. SPIE 7307, 730705-1-13 (2009)
[10] Christian A. Gueymard, “The sun’s total and spectral irradiance for solar energy applications and solar radiation models”, Solar Energy 76(4), 423-453 (2004)
[11] Breault Research Organization, “User Guide ; ASAP Reference Guide (2009)”, http://www.breault.com/k-base.php?kbaseID=216&catID=63, 1-617 (2009)
[12] Breault Research organization, “Scattering in ASAP”, http://www.breault.com/k-base.php?kbaseID=37&catID=44, 1-56 (2009)
[13] Christian A. Gueymard, “SMARTS code, version 2.9.5 for Windows User’s Manual”, Solar Consulting Servies, 1-50 (2005)
[14] Christian A. Gueymard, “SMARTS2, A Simple Model of the Atmospheric Radiative Transfer of Sunshine : Algorithms and Performance Assessment”, Florida Solar Energy Center FSEC-PF-270-95, 1-88 (1995)
[15] WCRP/IAMAP/RC, “A Preliminary Cloudless Standard Atmosphere for Radiation Computation”, WCP 112 WMO TD-No. 24, 1-xx, (1986)
[16] N. Braslau and J. V. Dave, “Effect of Aerosols on the Transfer of Solar Energy Through Realistic Model Atmosphere”, J. Appl. Meteorol 30, 601-619 (1973)
[17] EOS Project Science Office, “NASA Earth Observation Data Base”, http://neo.sci.gsfc.nasa.gov/Search.html, data (2010)
[18] Forest Resources Assessment, “Global Ecological Zoning for the Global Forest Resources Assessment 2000 Final Report”, http://www.fao.org/docrep/006/ad652e/ad652e00.HTM , 1-211 (2001)
[19] A. H. Strahler, J.-P. Muller and MODIS Science Team Members, “MODIS BRDF/Albedo Product : Algorithms Theoretical Basis Document Version 5.0”,ATBD MODIS 09, 1-53 (1999)
[20] Roselyne Lacaze, “POLDER-3/PARASOL Land Surface Algorithms Description”, POSTEL, 1-23 (2006)
[21] Lucht, W., C.B. Schaaf, and A.H. Strahler, “An Algorithm for the Retrieval of Albedo from Space Using Semiempirical BRDF Models”, IEEE Trans. Geosci. Remote Sens. 38, 977-998 (2000)
[22] Roujean , J. L., M. Leroy and P. Y. Deschamps, “A Bi-directional Reflectance Model of the Earth’s Surface for the Correction of Remote Sensing Data”, JGR 97 (18), 455- 468 (1992)
[23] Breon, F. M., F. Maignan, M. Leroy and I. Grant, “Analysis of Hot Spot Directional Signatures Measured from Space”, JGR 107(16), 282-296 (2002)
[24] NSIDC, “Total Ice-Covered Area and Extent”, http://nsidc.org/data/smmr_ssmi_ancillary/area_extent.html, data (2010)
[25] Teruyuki Nakajima, Masayuki Tanaka, “Effect of Wind-Generated Waves on the Transfer of Solar Radiation in the Atmosphere-Ocean System”, Journal of Quantitative Spectroscopy and Radiative Transfer 29 (6), 521-537 (1983)
[26] Reto Stockli, Eric Vermote, Nazmi Saleous, Robert Simmon, and David Herring, “The Blue Marble Next Generation – A true color earth dataset including seasonal dynamics from MODIS”, http://earthobservatory.nasa.gov/Features/BlueMarble/bmng.pdf, 1-13 (2005)

ACKNOWLEDGMENT

This research was supported by Basic Science Research Program through the National Research Foundation of Korea(NRF) funded by the Ministry of Education, Science and Technology (2010-0010778). We acknowledge the support of Breault Research Organization through the user licenses for Advanced System analysis Program (ASAP™) for ray tracing computation.